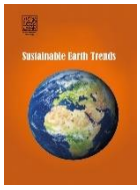
Sustainable Earth Trends 6(4) 2026 110-122

Shahid Beheshti University

Sustainable Earth Trends

Journal homepage: http://sustainearth.sbu.ac.ir



Synthesis of cerium oxide coated with semiconductor metals for photodegradation of amoxicillin and antibacterial activity from aqueous solutions

Mansoor Rahmani[a], Mohammad Hossein Sayadi[b*], Ayoob Rezaei[a]

[a] Department of Environmental Engineering, Faculty of Natural Resources and Environment, University of Birjand, Birjand, Iran
[b] Iranian National Institute for Oceanography and Atmospheric Science (INIOAS), Tehran 1411813389, Iran

ABSTRACT

Today, water pollution poses potential risks to human health and the environment. Recent research activities have focused on advanced oxidation processes (AOPs) as innovative technologies for water purification. Cerium oxide (CeO_2) is one of the most abundant rare earth oxides, which, when combined with other metals, creates an active surface and enhances photocatalytic properties. This study investigated the antibacterial properties and photocatalytic activity of cerium oxide nanoparticles combined with the semiconductors nickel and copper in the removal of organic pollutants (Amoxicillin) and antibacterial. The results showed that these nanocomposites have significant antibacterial properties at high concentrations. The optimal amount of the nanocomposite was found to be 0.7 mg/L, with a pH of 3 being the optimal condition for this experiment. Additionally, the optimal concentration of the pollutant was 5mg/L, which, in the presence of the nanocomposites $CuCo_2O_4/CeO_2$ and $NiCo_2O_4/CeO_2$, successfully removed 81% and 78% of the organic pollutant, respectively, under UV-A light exposure. The results of this study indicate that the synthesis of $CuCo_2O_4/CeO_2$ and $NiCo_2O_4/CeO_2$ nanoparticles serves as an effective antibacterial and highly photocatalytic material that can be used for the removal of organic pollutants and antibacterial. Considering the frequency of presence of organic pollutants and pathogens in the water environment, this research aims to strengthen CeO_2 with different morphologies by metals such as Cu and Ni so that they can act as recombination centers and increase its photocatalytic properties.

ARTICLE INFO

Keywords:
Antibacterial
Nanocomposite
Pharmaceutical pollution
Photodegradation

Article history:
Received: 05 March 2025
Accepted: 17 April 2025

*Corresponding author
E-mail address:
mh_sayadi@inio.ac.ir
(M.H. Sayadi)

Citation:
Rahmani, M. et al., (2026). Synthesis of cerium oxide coated with semiconductor metals for photodegradation of amoxicillin and antibacterial activity from aqueous solutions, *Sustainable Earth Trends:* 6(4), (110-122).

DOI: 10.48308/set.2025.239343.1115

1. Introduction

Water pollution poses potential risks to human health and the environment. Various pharmaceuticals and personal care products, endocrine disruptors, persistent organic pollutants and their metabolites are among the new emerging pollutants that cause direct and indirect harm and affect the health of all organisms (Pant et al., 2013). Contaminated water is a major cause of infectious diseases (such as malaria, cholera, amoebiasis, paratyphoid fever, and dysentery) (Alrumman et al., 2016). Epidemics caused by infectious agents in drinking water have previously occurred in most countries. The presence of microbiological pollutants, such as bacterial antibacterial in water sources, is one of the main causes of waterborne diseases like typhoid, dysentery, and cholera, which are significant causes of mortality (Kristanti et al., 2022), especially in developing countries. Therefore, disinfection is a critical step in the treatment of water and wastewater to ensure water safety. Conventional wastewater treatment plants often use chlorine and its derivatives. However, chlorination has limitations, such as the formation of harmful disinfection by-products (Qamar et al., 2021), thus creating a need for the development and use of suitable alternative disinfection techniques (Ikram et al., 2020). Advanced oxidation processes (AOPs), such as semiconductor photocatalysis, are suitable alternative disinfectants because they generate highly reactive hydroxyl radicals (·OH) that can attack and inactivate microorganisms without forming

Copyright: © 2026 by the authors. Submitted for possible open access publication under the terms and conditions of the Creative Commons Attribution (CC BY). license (https://creativecommons.org/licenses/by/4.0/).

DBPs (Qamar et al., 2021). However, AOPs have received considerable attention due to their bacterial inactivation rates. Unlike conventional water disinfection methods such as chlorination, ozonation, and ultraviolet radiation, AOPs are safer and more natural technologies for water disinfection (Nidheesh et al., 2022). They have many drawbacks, including high investments, maintenance costs, high consumption of chemical reagents, and environmental issues arising from the disposal of treated wastewater. In fact, chlorination leads to the production of carcinogenic by-products such as trihalomethanes (THMs). For ultraviolet radiation, many microorganisms can develop resistance. For ozonation, cost and safety concerns limit its practical use. The use of these methods can also result in the production of highly undesirable and toxic disinfection by-products (Alyani et al., 2019). Recent research activities have focused on advanced oxidation processes (AOPs) as potential innovative water purification technologies. AOPs rely on generating highly reactive transient species in situ for the mineralization of resistant organic compounds, neutralization of water antibacterial, and disinfection from by-products, using light or other forms of energy. Among AOPs, heterogeneous photocatalysis using semiconductor nanostructures has garnered attention as an efficient tool for degrading organic pollutants in water and air. Cerium oxide (CeO_2) is one of the most abundant rare earth oxides, often used in electrochemical cells, energy storage, optical devices, photocatalysis, and as a biomaterial (Chen et al., 2017). CeO_2 is an n-type semiconductor with various chemical and physical properties, such as pollutant removal without toxicity. The main feature of CeO_2 is the conversion of Ce^{4+} to Ce^{3+}, which leads to oxygen vacancies and high stoichiometric deviation, resulting in increased visible light absorption (Choudhary et al., 2020). Various reports on CeO_2 as a photocatalyst with different morphologies, such as nanocubes, nanowires, and nanodisks, are available using various templates. This study aims to produce CeO_2 nanomaterials with optimized mesoporous structures and controllable pore volumes. CeO_2 has also gained significant attention due to its antibacterial properties. A high level of antibacterial properties of CeO_2 has been achieved by tailoring its structural morphology, doping with various metals that activate its surface properties, or increasing its surface-to-volume ratio. However, pure CeO_2 is a weak photocatalyst due to its low surface area, low absorption in the visible range, and high bandgap energy (Montini et al., 2016). These shortcomings have been addressed by doping with rare earth metal ions to enhance photocatalytic degradation and improve the optical properties of doped CeO_2. Various metal ions (Co^{2+}, Zn^{2+}, Cd^{2+}) (Khan et al., 2017), non-metal ions (N, F, Br) (Wang et al., 2017), and noble metal ions (Ag^{2+}, Au^{2+}, Pt) (Zhou et al., 2018) have been incorporated for superior photocatalytic performance in metal oxides such as TiO_2 networks, utilizing the redox coupling of different oxidation states of transition metals that lead to surface redox activity. Zhou et al. (2016) reported the reduction of graphene oxide and TiO_2 nanotube arrays modified with cerium dioxide to achieve visible light-based photocatalytic performance. Dong et al. (2021) investigated the synthesis of $Pt@CeO_2@MoS_2$ with a hollow structure for the degradation of drugs and personal care products. Zhou et al. (2016) reported TiO_2 nanotube arrays modified with CeO_2 and reduced graphene oxide for the degradation of bisphenol. Amoresi et al. (2019) designed CeO_2 nanoparticles with various morphologies for better photocatalytic activity. Several reports on the doping of transition metals, such as Fe, Cu, and Cd in the CeO_2 lattice, create various defect sites that can act as recombination centers (Liyanage et al., 2014; Yang et al., 2017). The antibacterial activity of nanocomposites against both Gram-negative and Gram-positive bacteria has been extensively studied. Nanocomposites enhance antibacterial properties by altering the cell wall and membrane. For example, chitosan nanocomposites inhibit protein synthesis and mRNA by penetrating the nuclei of bacterial cells (Gopinath et al., 2015). Additionally, the presence of cerium oxide alongside chitosan acts as a supportive material and catalyst, capable of inhibiting and killing bacterial cells (Sanmugam et al., 2023). In another study, the use of $Ag@CeO_2$ nanocomposites showed that nanoparticles inhibit and kill bacteria by damaging the surface, wall, and membranes of bacterial cells, as well as by freezing cell wall proteins (Khan et al., 2014). In this research, the study focused on examining the antibacterial characteristics and photocatalytic effectiveness

of cerium oxide nanoparticles when modified with nickel and copper semiconductors for the elimination of organic pollutants and various antibacterial.

2. Material and methods

All chemicals used in this experiment, including hexahydrate cerium nitrate, sodium hydroxide, cobalt nitrate, copper nitrate, citric acid, acrylamide, nickel acetate, cerium chloride, glycine, and chitosan, were obtained from Merck, Germany, (all materials with a purity of 99%) and were of analytical grade. For the analysis of nanoparticles, XRD, TGA, and BET analyses were employed.

2.1. Synthesis of CeO_2

A 0.1 molar solution of hexahydrate cerium nitrate is prepared in 200 milliliters of deionized water, and a 0.3 molar solution of sodium hydroxide is prepared in 250 milliliters of deionized water. Titration of the $Ce(NO_3)_3$•H_2O solution is carried out using a burette and the sodium hydroxide solution. While titrating, the solution is stirred with a magnet to ensure uniformity. Then, to obtain the precipitate, centrifugation (Centurion Scientific-k2042 model) is performed (15 minutes at 8000 rpm), and the precipitate is washed with water and ethanol. Finally, the obtained precipitate is placed in a vacuum oven at 200 degrees Celsius to dry (Tumkur et al., 2021).

2.2. Synthesis of $CuCo_2O_4/CeO_2$ nanocomposites

Initially, $CuCo_2O_4$ nanoparticles are synthesized using the sol-gel method. Amounts of 0.58g of $Co(NO_3)_3 \cdot 6H_2O$ and 0.24 g of $Cu(NO_3)_2 \cdot 3H_2O$ are dissolved in 50 mL of C_2H_6O using a magnetic stirrer (Alpha Silver model) for 20 minutes. After the solution changes to a dark red color, 4.5 millimoles of citric acid are added. Then, acrylamide is gradually added to the solution, which is kept at 80 degrees Celsius until a gel is formed. The resulting powder is calcined for 5 hours at 350 degrees Celsius (He et al., 2021). To synthesize $CuCo_2O_4/CeO_2$ nanocomposites, 1g of CeO_2 is dissolved in 100 mL of C_2H_5OH. A nominal weight ratio of 4% $CuCo_2O_4$ is taken and added to the solution while stirring. The mixture is left at room temperature for 24 hours to dry. The resulting powder is then kept for 12 hours at 110 degrees Celsius and calcined for 3 hours at 550 degrees Celsius (Alzahrani et al., 2023).

2.3. Synthesis of $NiCo_2O_4/CeO_2$ nanocomposites

1 mole of nickel acetate ($Ni(CH_3COO)_2 \cdot 2H_2O$), (2-x) moles of cobalt nitrate ($Co(NO_3)_2 \cdot 6H_2O$), x moles of cerium chloride ($CeCl_3 \cdot 7H_2O$), 0.04 moles of glycine, and 0.01g of chitosan are dissolved in deionized water (x = 0.2, 0.4, 0.6, 0.8, 1) and then placed under magnetic stirring at 90 degrees Celsius until a sticky gel is obtained. The resulting gel is dried at 150 degrees Celsius. It is then held at 350 and 900 degrees Celsius for 4 and 22 hours, respectively, for calcination. Finally, for the synthesis of $NiCo_2O_4/CeO_2$ nanocomposite, the corresponding amount of cerium salt is mixed and ground well using a porcelain crucible (Santhosh et al., 2022).

2.4. Characterization techniques

The crystal structure of the synthesized nanoparticles was analyzed using X-ray diffraction (XRD, Rigaku Ultima IV). To investigate the changes in the chemical and physical behavior of the materials affected by temperature variations, thermal gravimetric analysis (TGA, STA6000) was utilized. Finally, for examining the adsorption of gas molecules on the surface of solid materials, BET analysis (Mini II) was used.

2.5. Experimental design for the destruction of organic pollutants from aqueous solutions

Initially, to determine the optimal pH of the solution, the organic pollutant in the experiments is adjusted to a concentration of 20 mg/L using 0.1 N sodium hydroxide and nitric acid solutions at various pH levels, with 0.5 g/L of catalyst over a period of 120 minutes. To investigate the optimal amount of catalyst, experiments will be conducted using varying amounts of the catalyst ranging from 0.1 to 1 g/L with a concentration of 25 mg/L of pollutant at the optimal pH over a period of 120 minutes. To determine the optimal concentration of the pollutant, solutions containing different amounts of this compound will be examined under the optimal pH and

optimal catalyst amount over a period of 120 minutes.

2.6. Investigation of antimicrobial activity of $CuCo_2O_4/CeO_2$ and $NiCo_2O_4/CeO_2$ nanocomposites

The antibacterial effects of $CuCo_2O_4/CeO_2$ and $NiCo_2O_4/CeO_2$ nanocomposites were examined using the disk diffusion method in Mueller-Hinton agar against the Gram-negative bacterium Escherichia coli and the Gram-positive bacterium Staphylococcus aureus (Mehata, 2021). For this purpose, the synthesized nanocomposites were prepared at concentrations of 250, 500, 750, and 1000 mcg/mL, and blank disks were soaked in these concentrations. After soaking the disks in the specified concentrations, they were placed in an oven for 24 hours to dry and then stored under sterile conditions. For microbial cultivation, a bacterial suspension was uniformly transferred onto Mueller-Hinton agar using a sterile swab (lawn culture). The disks containing the specified concentrations were placed on the culture medium at predetermined distances using sterile tweezers under sterile conditions. The plates were incubated at 37 degrees Celsius for 24 hours. The diameter of the inhibition zone created was measured using a ruler in millimeters. Finally, each experiment was repeated at least three times, and the average diameter of the inhibition zones was calculated.

3. Results and discussion

3.1. Photodegradation experiments

3.1.1. Effect of pH

The pH of the solution in experiments is another important factor and parameter in chemical reactions. The synthesized $CuCo_2O_4/CeO_2$ and $NiCo_2O_4/CeO_2$ nanocomposites were prepared for the degradation of amoxicillin at pH values of (3, 5, 7, 9, 11), and the results were examined. In this experiment, a specific amount of amoxicillin powder and a defined quantity of the nanocomposite were weighed and dissolved in 100 milliliters of aqueous solution. 0.1 molar NaOH and HCl were used to adjust the pH. Before placing the samples under UV-A light, they were kept in the dark for 30 minutes and then exposed to the UV-A reactor for the specified duration. Fig. 1 shows the percentage of amoxicillin removal over different time intervals, indicating that the highest photocatalytic degradation occurred at the lowest pH (pH=3) and the longest duration under UV-A light. As shown in the graphs, due to the acidic conditions and the presence of electron pairs on the pollutant, a magnetic environment can be created for the removal of negatively charged pollutants using positively charged nanocomposites. In general, the pH of the solution can influence the photocatalytic activity based on the type of substrate and the surface properties of the photocatalytic nanocomposite. This effect was also observed in the study by Rashki and colleagues in 2022, where they removed pesticides through photocatalytic processes. It was noted that the highest removal rate occurred under acidic conditions, which is primarily due to the formation of OH^+ radicals during the process (Rashki et al., 2022). Tetracycline was also removed by Ha and colleagues in an aqueous medium at pH 2 (Ha et al., 2022). During this experiment, it was concluded that the highest removal rate was observed at acidic pH.

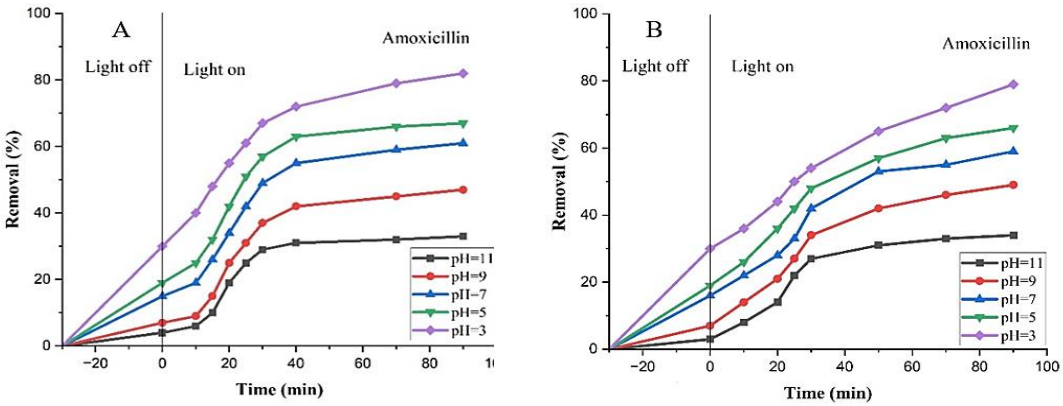


Fig. 1. Effect of pH on the removal of amoxicillin (Amoxicillin concentration= 50mg/L, and catalyst dosage = 0.5 g/L) by $CuCo_2O_4/CeO_2$ (A) and $NiCo_2O_4/CeO_2$ (B).

3.1.2. Effect of catalyst amount

The effect of catalyst dosage on photocatalytic degradation was studied at amounts of 0.1, 0.3, 0.5, 0.7, and 1 g/L liter. It was found that 0.7 g/L of catalyst is the optimal amount for efficient degradation of the pollutant. As shown in Fig. 2, with the increase in catalyst amount, the number of cerium oxide particles and active sites also increases, resulting in enhanced pollutant removal. However, excessive increases beyond the optimal amount will no longer affect pollutant removal. Additionally, as the catalyst amount increases, the number of active surface sites decreases, and light scattering occurs unfavorably, which in turn reduces light transmission and penetration (Pirilä et al., 2015). The optimal amount of catalyst was obtained at 0.7 mg/L, and increasing its concentration not only did not affect the removal of amoxicillin, but also led to undesirable light scattering, reducing the active sites on the surface and light penetration (Chong et al., 2010). according to a study by Sayadi and colleagues, azithromycin at a concentration of 1 g/L of GO@Fe_3O_4/ZnO/SnO_2 catalyst was able to decompose 90% of this pollutant under UV-C irradiation (Sayadi et al., 2019).

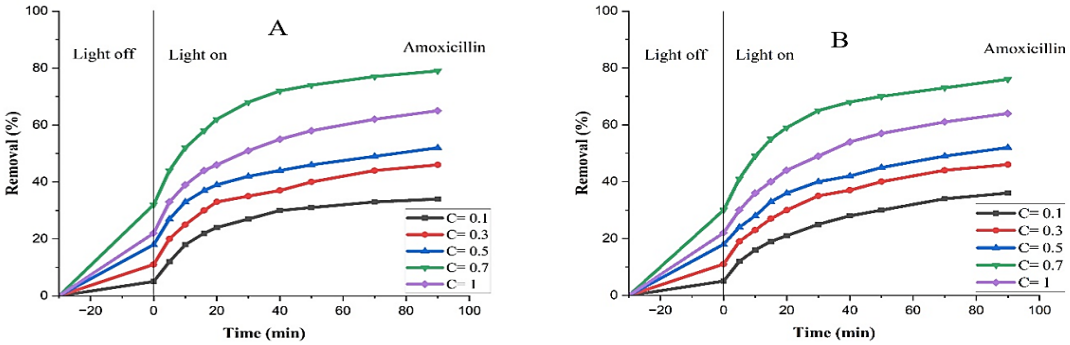


Fig. 2. Effect of catalyst dosage on pollutant removal (Amoxicillin concentration = 50mg/L and pH = 3): $CuCo_2O_4/CeO_2$ (A) and $NiCo_2O_4/CeO_2$ (B).

3.1.3. Effect of organic pollutant concentration

Organic pollutant samples were prepared at different concentrations (ranging from 5 to 100 mg/L), and the optimal pH and catalyst were placed for 90 min before conducting the experiment. Before placing the samples under UV-A light, the solutions were kept in the dark for 30 min to establish equilibrium between the catalyst and the pollutant, after which the samples were read in the spectrophotometer, as shown in Fig. 3. The degradation efficiency of amoxicillin at a concentration of 5 mg/L in the presence of the $CuCo_2O_4/CeO_2$ catalyst was 81%, while the lowest efficiency at 100 mg/L was 28%. The highest degradation efficiency in the presence of the $NiCo_2O_4/CeO_2$ catalyst was found to be 78%. Therefore, it can be concluded that as the concentration increases, the available sites decrease, resulting in a lower removal percentage (Khashi et al., 2023). In addition, the presence of nanoparticles in the presence of UV-A light increases photocatalytic reactions and, due to the creation of electron holes, further activates the nanoparticles. It also helps to decompose pollutants by producing free radicals and can remove toxic compounds from the environment (Bodzek, 2022). It is important to note that under optimal concentrations without the use of a catalyst, a removal rate of 18.4% was achieved through photolysis in just 30 minutes.

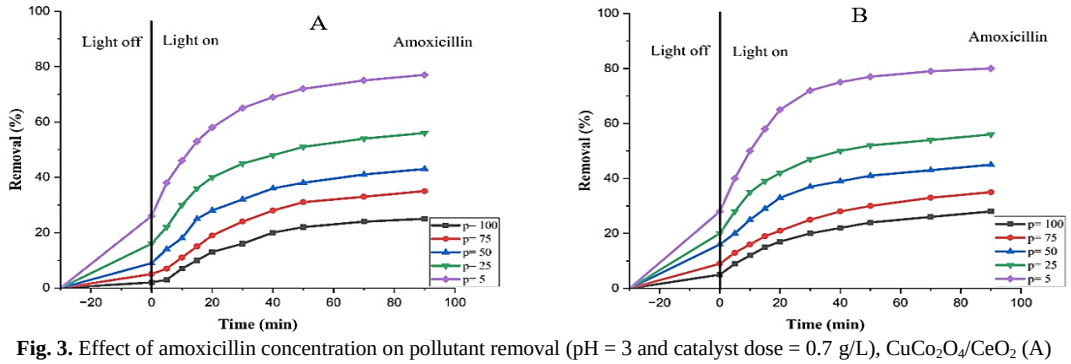


Fig. 3. Effect of amoxicillin concentration on pollutant removal (pH = 3 and catalyst dose = 0.7 g/L), $CuCo_2O_4/CeO_2$ (A) and $NiCo_2O_4/CeO_2$ (B).

3.2. Photocatalytic degradation kinetics of amoxicillin

In photocatalytic processes, the kinetics of degradation over time for the pharmaceutical pollutant amoxicillin is examined and shown in Fig. 4 and Tables 1. In this study, the optimal experimental conditions included a pH of 3, a concentration of 25 mg/L of the amoxicillin, and 0.7 g/L of the nanocomposite, subjected to UV-A light for a duration of 10 to ۸0 min. The reaction kinetics were calculated using the following equation (Chamanehpour et al., 2023) (Eq. 1):

$$Ln\left(\frac{C0}{Ct}\right) = Kt \qquad (1)$$

Where K is the reaction rate constant, C_0 is the initial concentration of the pollutant, and C_t is the concentration of the pollutant at time t.

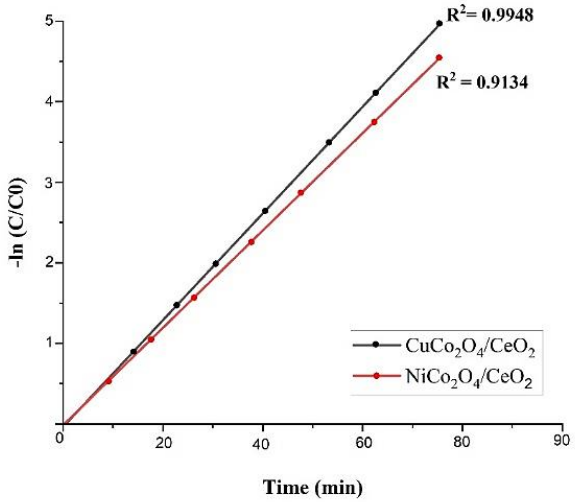


Fig. 4. Kinetics of photocatalytic degradation of amoxicillin in the presence of $CuCo_2O_4/CeO_2$ and $NiCo_2O_4/CeO_2$.

According to the results obtained (first-order kinetics with high linear regression coefficient) (Nguyen et al., 2019), the degradation of amoxicillin with both $CuCo_2O_4/CeO_2$ and $NiCo_2O_4/CeO_2$ catalysts can be carried out with UV light. In the experimental conditions for both nanocomposites, a concentration of 0.7 mg/L nanoparticles, pH 3, and a contaminant concentration of 5 mg/L, the degradation rate of amoxicillin reached 81% and 78% after 80 minutes of irradiation.

Table 1. Kinetic data related to the amoxicillin pollutant in the presence of nanocomposites $CuCo_2O_4/CeO_2$ and $NiCo_2O_4/CeO_2$.

Nanocomposite Type	Amoxicillin concentration mg/L	Equation	K0 $(min)^{-1}$	R^2
$CuCo_2O_4/CeO_2$	5	Y=0.0143x+1.4829	0.0143	0.9948
	25	Y=0.0152x+1.0230	0.0152	0.9857
	50	Y=0.0138x+0.9310	0.0138	0.9862
	75	Y=0.0196x+0.7020	0.0196	0.9974
	100	Y=0.0149x+0.9004	0.0149	0.9935
$NiCo_2O_4/CeO_2$	5	Y=0.0142x+2.308	0.0142	0.9134
	25	Y=0.0141x+2.313	0.0141	0.8957
	50	Y=0.0140x+2.318	0.0140	0.8762
	75	Y=0.0139x+2.323	0.0139	0.8574
	100	Y=0.0138x+2.328	0.0138	0.8335

3.3. Characterization of nanoparticles

3.3.1. XRD

The XRD pattern is shown in the Fig. 5. In the left figure, CeO_2 exhibits peaks at 28, 47, 56, 58, and 69 degrees, indicating the presence of crystal planes (111), (220), (311), (222), and (400), which correspond to the standard card (JCPDS card number 34-0394). This nanoparticle has a cubic fluorite structure (Tumkur et al., 2021). $CuCo_2O_4$ also shows peaks at 31, 38, 44, 60, and 65 degrees, corresponding to the crystal planes (220), (222), (400), (511), and (440), in accordance with the standard card (JCPDS no.: 71-0816) (Zheng et al., 2020). The peaks observed in the $CuCo_2O_4/CeO_2$ nanocomposite indicate that all peaks present in the synthesized sample are retained, with slight variations compared to CeO_2. However, peaks at 31, 36, 45, 55, 59, and 65, corresponding to the spinel crystal planes (220), (311), (400), (511), and (440), align with the standard card (JCPDS NO.71-1887) (Liu et al., 2021). In the right figure, the two predominant phases are CeO_2 and $NiCo_2O_4$. $NiCo_2O_4$ shows 2θ values at 31, 38, 43, and 65, corresponding to the crystal planes (220), (222), (400), and (440), in accordance with the standard card (JCPDS 20-0781). The diagram of $NiCo_2O_4/CeO_2$ confirms the combination of these two nanoparticles to form metal oxides (Fu et al., 2019). Using the Scherrer Eq. 2:

$$D = (0.943 \times \lambda)/(\beta \times COS\theta) \quad (2)$$

The sizes of $CuCo_2O_4$ and $NiCo_2O_4$ nanoparticles were approximately 17 and 23 nm, respectively (Xiao et al., 2019; Franklin et al., 2024).

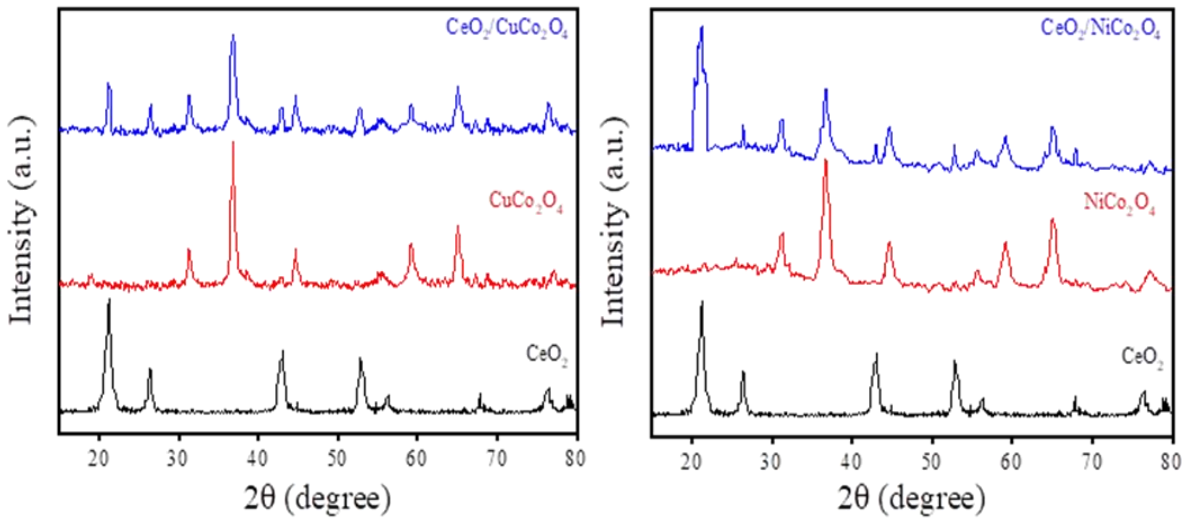


Fig. 5. The XRD pattern corresponds to the $NiCo_2O_4/CeO_2$ and $CuCo_2O_4/CeO_2$ nanocomposite.

3.3.2. TGA

In Fig. 6, the black graph represents TGA, and the red graph represents DTG, which measures the changes in the sample's mass due to increasing temperature. The left figure corresponds to the $NiCo_2O_4/CeO_2$ nanocomposite, showing a final weight loss of 28.45% observed in the range of 800 to 1000 degrees Celsius. This weight change is due to the removal of hydroxyl groups and the oxidation of nickel and cobalt from the nanocomposite, and the DTG curve corresponds to the TGA curve (Venkatachalam et al., 2017). The right figure corresponds to the $CuCo_2O_4/CeO_2$ nanocomposite, where two stages of weight loss are observed. The first weight loss occurs in the range of 200 to 400 degrees Celsius, related to the sublimation of material, and the second weight loss occurs in the range of 800 to 1000 degrees Celsius due to the decomposition of volatile products, reaching a weight change of 35.06% with temperature variation (Xiao et al., 2019). The peaks observed in both graphs are endothermic peaks, which may be related to the spinel structure of the two nanocomposites and their oxidation processes.

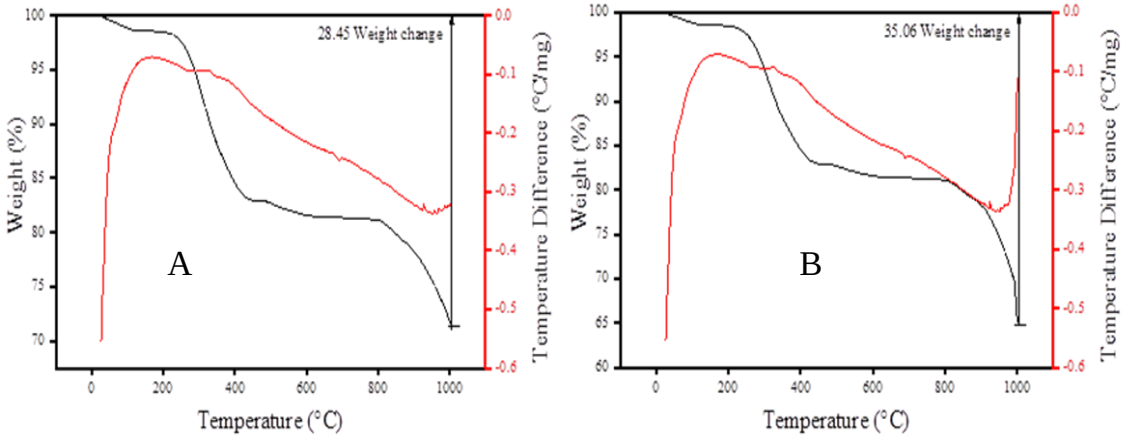


Fig. 6. The black curve represents Thermal Gravimetric Analysis (TGA) and the red curve represents Differential Thermal Analysis (DTG) for the two nanocomposites $CuCo_2O_4/CeO_2$ (A) and $NiCo_2O4/CeO_2$ (B).

3.3.3. BET

BET analysis is one of the methods for measuring and examining surface porosity, which is measured through the adsorption/desorption of nitrogen. This analysis shows (Fig. 7) that the $CuCo_2O_4$ nanoparticle has pores, a large surface area, mesoporous material characteristics, and an IV isotherm with an H_2-type hysteresis loop. As a result, it provides more active catalytic sites. The $CuCo_2O_4$ nanowire has a significant surface area, but the introduction of CeO_2 reduces the pore size and surface area. The average pore diameter, calculated using the BJH method, is 6.30 nanometers. The value of as is equal to 93.06 m^2/ g, indicating that this high surface area and the presence of a mesoporous structure increase active sites, facilitating rapid mass transfer and excellent electrochemical properties. The three endothermic peaks present in the B curve indicate that the decomposition process consists of three stages. Overall, it can be concluded that the thermal decomposition process shows significant changes after mixing CeO_2 with $CuCo_2O_4$ (Xiao et al., 2019). The large surface area of the $CuCo_2O_4/CeO_2$ nanocomposites, along with their mesoporous structures, enhances the adsorption and diffusion of catalysts, leading to improved photocatalytic capabilities.

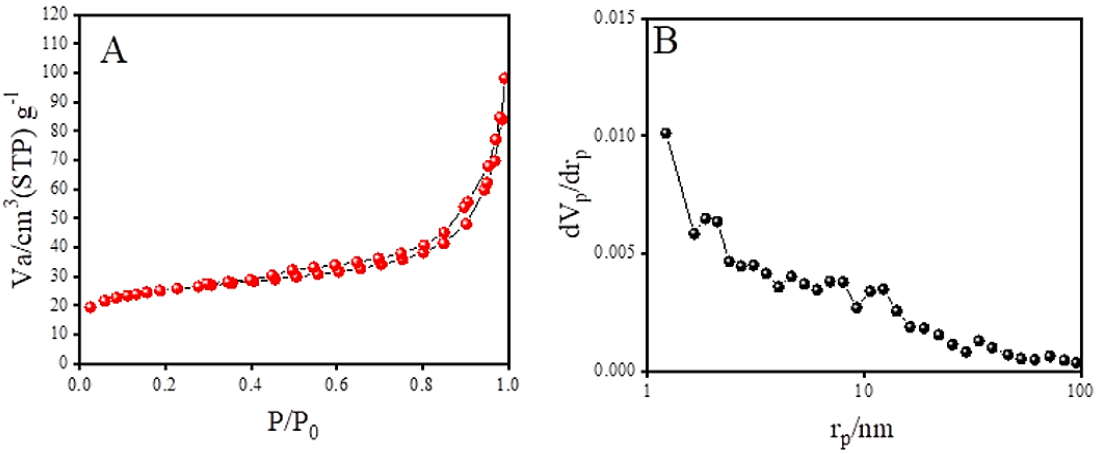


Fig. 7. Nitrogen adsorption/desorption isotherm (A) and (B) BJH plot of pore size distribution for the $CuCo_2O_4/CeO_2$ sample.

Fig. 8A shows the curve of the isotherm measured for the $NiCo_2O_4/CeO_2$ nanoparticle, which indicates a type III isotherm curve with an H3-type hysteresis loop. The BET surface area is approximately 6.60 m^2/g. In this nanocomposite, there is a weak interaction between particles (adsorbent-adsorbent), consisting of aggregates with a plate-like structure and slit-like pores. Fig. 8B also represents the BJH plot, which illustrates the pore size distribution in a porous structure, with an average pore diameter observed to be 41.70 nanometers using this method (Santhosh et al., 2022).

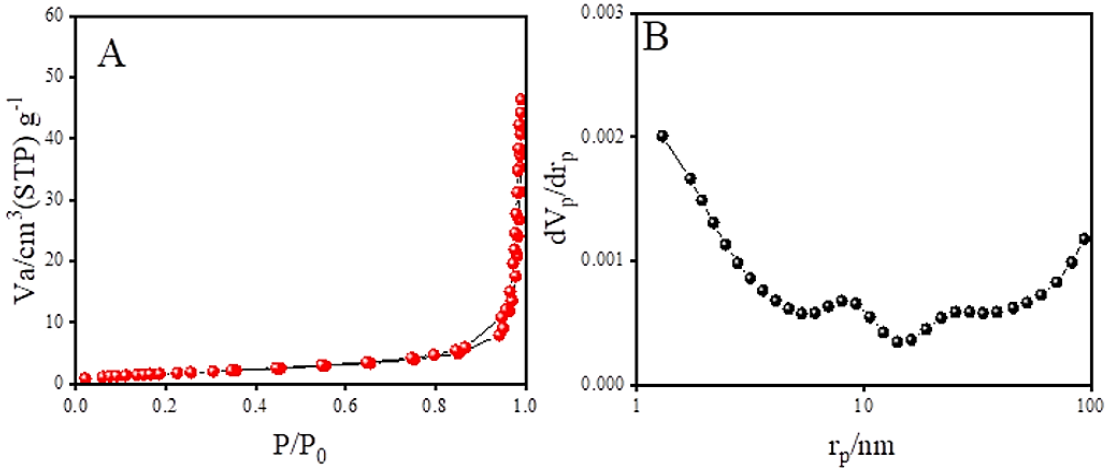


Fig. 8. (A) Nitrogen adsorption/desorption isotherm and (B) BJH plot of pore size distribution for the $NiCo_2O_4/CeO_2$ sample.

3.4. Reuse of nanocomposites $CuCo_2O_4/CeO_2$ and $NiCo_2O_4/CeO_2$

Examining and testing the stability and reusability of the catalyst is highly important for saving costs, energy, and ultimately ensuring the efficiency and practical performance of the catalyst. After each use of the nanocomposite, the catalyst was collected using centrifugation and then washed and dried in an oven for reuse. The results are shown in Fig. 9, where four cycles were evaluated for the recycling of the nanocatalyst. For the $CuCo_2O_4/CeO_2$ catalyst, the pollutant degradation percentage decreased from 81% in the first cycle to 69% in the fourth cycle; For the $NiCo_2O_4/CeO_2$ catalyst, the pollutant degradation percentage decreased from 78% in the first cycle to 65% in the fourth cycle; this demonstrates the high stability of the nanocomposites.

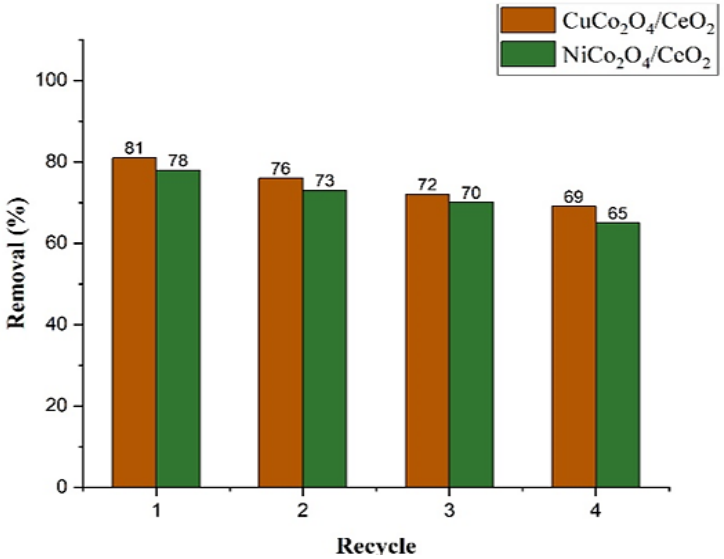


Fig. 9. Efficiency and stability in the reuse of the $CuCo_2O_4/CeO_2$ and $NiCo_2O_4/CeO_2$ nanocomposites.

3.4. Antibacterial Effect of $CuCo_2O_4/CeO_2$ and $NiCo_2O_4/CeO_2$ nanocomposites

The results of the antibacterial activity of the synthesized $CuCo_2O_4/CeO_2$ and $NiCo_2O_4/CeO_2$ nanocomposites are shown in Fig. 10. Based on these results, for the Gram-negative bacterium Escherichia coli, a significant antibacterial activity was observed at a concentration of 2000 mcg/mL, with the diameter of the inhibition zone measuring 11 and 8 millimeters, respectively. As the concentration of the nanocomposites decreased, the size of the inhibition zone also decreased, such that at a concentration of 1000 mcg/mL, the diameter of the inhibition zone for the $CuCo_2O_4/CeO_2$ and $NiCo_2O_4/CeO_2$ nanocomposites was recorded as 9 and 6 millimeters, respectively. For the Gram-positive bacterium Staphylococcus aureus, at a concentration of 2000 mcg/mL, the diameter of the inhibition zone for the

$CuCo_2O_4/CeO_2$ and $NiCo_2O_4/CeO_2$ nanocomposites was found to be 9 and 7 millimeters, respectively. Similarly, with a decrease in concentration to 1000 mcg/mL, the diameter of the inhibition zone decreased, yielding values of 7 and 4 millimeters for $CuCo_2O_4/CeO_2$ and $NiCo_2O_4/CeO_2$, respectively. Overall, as the concentration of the synthesized nanocomposites decreased, their antibacterial properties also diminished, such that at a concentration of 250 mcg/mL, no antibacterial activity was observed (Table 2).

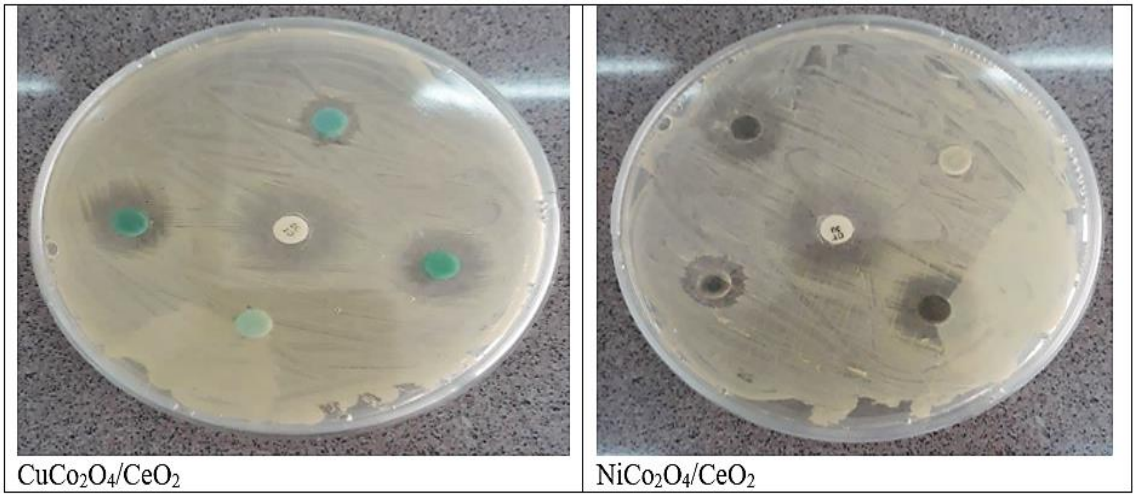


Fig. 10. Inhibition zones of *Escherichia coli* and *Staphylococcus aureus* in the presence of nanocomposites.

Table 2. Diameter of the inhibition zone of bacteria (millimeters).

Nanocomposite	Bacteria	Gentamicin control	2000 µg/ml	1000 µg/ml	500 µg/ml	250 µg/ml
$CuCo_2O_4/CeO_2$	*E. coli*	13	11	9	6	0
$NiCo_2O_4/CeO_2$	*E. coli*	13	8	6	3	0
$CuCo_2O_4/CeO_2$	*S. aureus*	11	9	7	4	0
$NiCo_2O_4/CeO_2$	*S. aureus*	11	7	4	2	0

By comparing the results of the antibacterial activity of the $CuCo_2O_4/CeO_2$ and $NiCo_2O_4/CeO_2$ nanocomposites, it can be observed that these nanocomposites exhibit significant antibacterial properties at high concentrations. At a concentration of 2000 mcg/mL, these compounds effectively demonstrated the ability to eliminate Staphylococcus aureus and Escherichia coli bacteria. Due to the unique characteristics of nanomaterials, including a higher surface-to-volume ratio and more effective adsorption, nanocomposites have high efficiency and effectiveness in terms of antibacterial activity (Shekari et al., 2017). It is noteworthy that as the concentration of the nanocomposites decreases, their antimicrobial properties also diminish. With a decrease in particle size, the potential for the release of element ions also increases. The synthesized nanocomposites, due to their large particle size and contact surface, have greater exposure to microorganisms, which leads to enhanced biological and chemical activities, ultimately having a more pronounced effect on bacterial cell membranes. In addition to particle size, the concentration of the nanocomposites also plays an important role in their antimicrobial properties. At low concentrations, the limited number of nanocomposite particles reduces their interaction with bacterial cell membranes, leading to decreased inhibitory power and, consequently, a reduction in bactericidal activity and the diameter of the inhibition zone. Research by Azizi and colleagues showed that at low concentrations, $ZnS/WO_3/Ag$ and $ZnS/WO_3/Pd$ nanocomposites exhibited lower antibacterial properties; however, as the concentration increased, their antibacterial activity was significantly enhanced, resulting in the formation of a larger inhibition zone (Azizi et al., 2024). Therefore, to effectively combat bacterial growth, selecting a balanced and appropriate concentration of nanocomposites is

crucial to achieve optimal and effective performance. In a study conducted by Abdollahzadeh and colleagues on the MOF-CS/GO nanocomposite, the results indicated that the synthesized nanocomposite, at an appropriate concentration, exhibited exceptional antibacterial properties against Staphylococcus aureus and Escherichia coli (Abdollahzadeh et al., 2023).

4. Conclusion

Based on the analysis of TGA, the presence of endothermic peaks and the spinel structure in these nanocomposites relates to their oxidation process. Additionally, the XRD analysis confirmed their spinel structure and cubic fluorite due to the presence of cerium oxide nanoparticles, while the BET analysis confirmed the mesoporous characteristics and large surface area. During the photocatalytic process, three parameters pH, concentration of organic pollutant, and catalyst dose were examined. According to the results, the effect of pH = 3 on the nanocomposites indicates that under acidic conditions, the electron pairs interact with the pollutant, allowing the nanocomposite to create a magnetic environment for removing negatively charged pollutants with positively charged nanocomposites. The results showed that at a concentration of 5 mcg/L of organic pollutant in the presence of the $CuCo_2O_4/CeO_2$ and $NiCo_2O_4/CeO_2$ catalysts, the degradation efficiency of amoxicillin was 81% and 78%, respectively. Furthermore, a concentration of 0.7 g/L of catalyst was found to be optimal for the efficient degradation of the pollutant. Overall, the results of this study indicate that the synthesis of $CuCo_2O_4/CeO_2$ and $NiCo_2O_4/CeO_2$ nanoparticles serves as an effective antibacterial and highly photocatalytic material that can be used for the removal of organic pollutants.

Acknowledgment

The paper is from a PhD student thesis in the Department of Environmental Engineering, Faculty of Natural Resources and Environment, University of Birjand. Thereby the authors appreciate the assistance of laboratories in the Faculty of Natural Resources and Environment, University of Birjand, during the course of the experiments and analysis. We also thank Mr. Shekari, and the University of Birjand Department of Natural Resources and Environment for their valuable support in laboratory analysis.

Reference

Abdollahzadeh, S., Sayadi, M.H. & Shekari, H., 2023. Synthesis of biodegradable antibacterial nanocomposite (metal–organic frameworks supported by chitosan and graphene oxide) with high stability and photocatalytic activities. *Inorganic Chemistry Communications*, *156*, 111302.

Alrumman, S., Keshk, S. & El Kott, A., 2016. Water pollution: source & treatment. *American Journal of Environmental Engineering*, 88-98.

Alyani, S.J., Pirbazari, A.E., Khalilsaraei, F.E., Kolur, N.A. & Gilani, N.J., 2019. Growing Co-doped TiO_2 nanosheets on reduced grapheme oxide for efficient photocatalytic removal of tetracycline antibiotic from aqueous solution and modeling the process by artificial neural network. *Journal of Alloys and Compounds*, 799, 169–182.

Alzahrani, K.A., Ismail, A.A. & Alahmadi, N., 2023. CuCo2O4/CeO2 S-scheme photocatalyst for promoted CO_2 photoreduction to CH3OH. *Journal of Molecular Liquids*, 376, 121509.

Amoresi, R.A., Oliveira, R.C., Marana, N.L., De Almeida, P.B., Prata, P. S., Zaghete, M.A. ... & Simoes, A. Z., 2019. CeO_2 nanoparticle morphologies and their corresponding crystalline planes for the photocatalytic degradation of organic pollutants. *ACS Applied Nano Materials*, 2(10), 6513-6526.

Azizi, R., Sayadi, M.H. & Shekari, H., 2024. Evaluation of multifunctional ZnS/WO3 nanocomposites enhanced with palladium and silver for pollutant degradation and antibacterial applications. *Journal of Water Process Engineering*, 67, 106143.

Bodzek, M., 2022. Nanoparticles for water disinfection by photocatalysis: A review. *Archives of Environmental Protection*, 48(1), 3-17.

Chamanehpour, E., Sayadi, M.H. & Hajiani, M., 2023. Metal-organic framework coordinated with g-C3N4 and metal ions for boosting photocatalytic H2 production under sunlight. *Journal of Photochemistry and Photobiology A: Chemistry*, 434, 114221.

Chen, F., Ho, P., Ran, R., Chen, W., Si, Z., Wu, X. ... & Lee, C., 2017. Synergistic effect of CeO2 modified TiO2 photocatalyst on the enhancement of visible light photocatalytic performance. *Journal of Alloys and Compounds*, 714, 560-566.

Chong, M.N., Jin, B., Chow, C.W. & Saint, C., 2010. Recent developments in photocatalytic

water treatment technology: a review. *Water Research*, 44(10), 2997-3027.

Choudhary, S., Sahu, K., Bisht, A., Singhal, R. & Mohapatra, S., 2020. Template-free and surfactant-free synthesis of CeO2 nanodiscs with enhanced photocatalytic activity. *Applied Surface Science*, 503, 144102.

Dong, C., Zheng, Z., Badsha, M.A., He, J. & Lo, I. M., 2021. Visible-light-driven peroxymonosulfate activation in photo-electrocatalytic system using hollow-structured Pt@ CeO_2@ MoS_2 photoanode for the degradation of pharmaceuticals and personal care products. *Environment International*, 154, 106572.

Franklin, J.B., Saravanan, P., Suruthi, S., Bincy, F.I.M., Sundaram, S. J., Dhas, S.M.B. ... & Mythili, R., 2024. Impact of shock compression on the photovoltaic performance of $NiCo_2O_4$ Nanoparticles. *Luminescence*, 39(12), e70043.

Fu, H., Liu, Y., Chen, L., Shi, Y., Kong, W., Hou, J. ... & Guo, X., 2019. Designed formation of $NiCo_2O_4$ with different morphologies self-assembled from nanoparticles for asymmetric supercapacitors and electrocatalysts for oxygen evolution reaction. *Electrochimica Acta*, 296, 719-729.

Gopinath, K., Karthika, V., Sundaravadivelan, C., Gowri, S. & Arumugam, A., 2015. Mycogenesis of cerium oxide nanoparticles using Aspergillus niger culture filtrate and their applications for antibacterial and larvicidal activities. *Journal of Nanostructure in Chemistry*, 5, 295-303.

Ha, G.H., Mohan, H., Oh, H.S., Kim, G., Seralathan, K.K. & Shin, T., 2022. Photocatalytic degradation of tetracycline using hybrid Ag/Ag_2S@ BiOI nanowires: Degradation mechanism and toxicity evaluation. *Chemosphere*, *303*, 135091.

He, Z., Yang, H., Su, J., Xia, Y., Fu, X., Kang, L. ... & Wu, M., 2021. Polyacrylamide gel synthesis and photocatalytic performance of $CuCo_2O_4$ nanoparticles. *Materials Letters*, 288, 129375.

Ikram, M., Raza, A., Imran, M., Ul-Hamid, A., Shahbaz, A., Ali, S.J., 2020. Hydrothermal synthesis of silver decorated reduced grapheme oxide (rGO) nanoflakes with effective photocatalytic activity for wastewater treatment. *Nanoscale Research Letters*. 15(1), 95.

Khan, M.M., Ansari, S.A., Lee, J.H., Ansari, M.O., Lee, J. & Cho, M.H., 2014. Electrochemically active biofilm assisted synthesis of Ag@CeO_2 nanocomposites for antimicrobial activity, photocatalysis and photoelectrodes. *Journal of Colloid and Interface Science*, 431, 255-263.

Khan, M.M., Khan, W., Ahamed, M. & Alhazaa, A. N., 2017. Microstructural properties and enhanced photocatalytic performance of Zn doped CeO_2 nanocrystals. *Scientific Reports*, 7(1), 12560.

Khashi, N. & Sayadi, M.H., 2023. In_2O_3/NIO/MOS_2 Composite as a novel photocatalytic towards imatinib and 5-fluorouracil degradation. *Water*, 15(18), 3263.

Kristanti, R.A., Hadibarata, T., Syafrudin, M., Yılmaz, M. & Abdullah, S., 2022. Microbiological contaminants in drinking water: Current status and challenges. *Water, Air, & Soil Pollution*, 233(8), 299.

Liyanage, A.D., Perera, S.D., Tan, K., Chabal, Y. & Balkus Jr, K.J., 2014. Synthesis, characterization, and photocatalytic activity of Y-doped CeO_2 nanorods. *Acs Catalysis*, 4(2), 577-584.

Mehata, M.S., 2021. Green synthesis of silver nanoparticles using Kalanchoe pinnata leaves (life plant) and their antibacterial and photocatalytic activities. *Chemical Physics Letters*, 778, 138760.

Montini, T., Melchionna, M., Monai, M. & Fornasiero, P., 2016. Fundamentals and catalytic applications of CeO2-based materials. *Chemical Reviews*, 116(10), 5987-6041.

Nguyen, T.T., Nam, S.N., Son, J. & Oh, J., 2019. Tungsten trioxide (WO_3)-assisted photocatalytic degradation of amoxicillin by simulated solar irradiation. *Scientific Reports*, 9(1), 9349.

Nidheesh, P.V., Divyapriya, G., Titchou, F.E. & Hamdani, M., 2022. Treatment of textile wastewater by sulfate radical based advanced oxidation processes. *Separation and Purification Technology*, 293, 121115.

Pant, B., Pant, H.R., Barakat, N.A.M., Park, M., Jeon, K., Choi, Y. & Kim, H.-Y., 2013. Carbon nanofibers decorated with binary semiconductor (TiO_2/ZnO) nanocomposites for the e_ective removal of organic pollutants and the enhancement of antibacterial activities. *Ceramics International*, 39(6), 7029-7035.

Pirilä, M., Saouabe, M., Ojala, S., Rathnayake, B., Drault, F., Valtanen, A., ... & Keiski, R. L., 2015. Photocatalytic degradation of organic pollutants in wastewater. *Topics in Catalysis*, 58, 1085-1099.

Qamar, M.A., Shahid, S., Javed, M., Sher, M., Iqbal, S., Bahadur, A. & Li, D., 2021. Fabricated novel g-C_3N_4/Mn doped ZnO nanocomposite as highly active photocatalyst for the disinfection of pathogens and degradation of the organic pollutants from wastewater under

sunlight radiations. *Colloids and Surfaces A: Physicochemical and Engineering Aspects*, 611, 125863.

Rashki, O., Rezaei, M.R. & Sayadi, M. H., 2022. The high photocatalytic efficiency and stability of the Z-scheme $CaTiO_3/WS_2$ heterostructure for photocatalytic removal of 17α-ethinyl estradiol in aqueous solution. *Journal of Photochemistry and Photobiology A: Chemistry*, 433, 114169.

Sanmugam, A., Abbishek, S., Kumar, S.L., Sairam, A.B., Palem, V.V., Kumar, R.S. ... & Vikraman, D., 2023. Synthesis of chitosan based reduced graphene oxide-CeO2 nanocomposites for drug delivery and antibacterial applications. *Journal of the Mechanical Behavior of Biomedical Materials*, 145, 106033.

Santhosh, G., Nayaka, G.P. & Bhatt, A.S., 2022. Ultrahigh capacitance of $NiCo_2O4/CeO_2$mixed metal oxide material for supercapacitor applications. *Journal of Alloys and Compounds*, 899, 163312.

Sayadi, M.H., Sobhani, S. & Shekari, H., 2019. Photocatalytic degradation of azithromycin using $GO@Fe_3O_4/ZnO/SnO_2$ nanocomposites. *Journal of Cleaner Production*, 232, 127-136.

Shekari, H., Sayadi, M.H., Rezaei, M.R. & Allahresani, A., 2017. Synthesis of nickel ferrite/titanium oxide magnetic nanocomposite and its use to remove hexavalent chromium from aqueous solutions. *Surfaces and Interfaces*, 8, 199-205.

Tumkur, P.P., Gunasekaran, N.K., Lamani, B.R., Nazario Bayon, N., Prabhakaran, K., Hall, J.C. & Ramesh, G.T., 2021. Cerium oxide nanoparticles: Synthesis and characterization for biosafe applications. *Nanomanufacturing*, 1(3), 176-189.

Venkatachalam, V., Alsalme, A., Alghamdi, A. & Jayavel, R., 2017. Hexagonal-like $NiCo_2O_4$ nanostructure based high-performance supercapacitor electrodes. *Ionics*, 23, 977-984.

Wang, Q., Zhu, S., Liang, Y., Cui, Z., Yang, X., Liang, C. & Inoue, A., 2017. One-step synthesis of size-controlled Br-doped TiO_2 nanoparticles with enhanced visible-light photocatalytic activity. *Materials Research Bulletin*, 86, 248-256.

Xiao, X., Zhang, Z., Cai, L., Li, Y., Yan, Z. & Wang, Y., 2019. The excellent catalytic activity for thermal decomposition of ammonium perchlorate using porous $CuCo_2O_4$ synthesized by template-free solution combustion method. *Journal of Alloys and Compounds*, 797, 548-557.

Yang, K., Li, D.F., Huang, W.Q., Xu, L., Huang, G.F. & Wen, S., 2017. Origin of enhanced visible-light photocatalytic activity of transition-metal (Fe, Cr and Co)-doped CeO_2: effect of 3 d orbital splitting. *Applied Physics A*, 123, 1-11.

Zhou, Q., Ma, S. & Zhan, S., 2018. Superior photocatalytic disinfection effect of Ag-3D ordered mesoporous CeO_2 under visible light. *Applied Catalysis B: Environmental*, 224, 27-37.

Zhou, Q., Xing, A., Zhao, D. & Zhao, K., 2016. Tetrabromobisphenol A photoelectrocatalytic degradation using reduced graphene oxide and cerium dioxide comodified TiO_2 nanotube arrays as electrode under visible light. *Chemosphere*, 165, 268-276.